SPRITE MRI of bubbly flow in a horizontal pipe

Mark Sankey [a], Zhi Yang [b], Lynn Gladden [a], Michael L. Johns [a], Derek Lister [c], Benedict Newling [b,*]

[a] Magnetic Resonance Research Centre, Department of Chemical Engineering & Biotechnology, University of Cambridge, Pembroke Street, Cambridge CB2 3RA, UK
[b] UNB MRI Centre, Department of Physics, University of New Brunswick, P.O. Box 4400, 8 Bailey Drive, Fredericton, NB, Canada E3B 5A3
[c] Department of Chemical Engineering, University of New Brunswick, P.O. Box 4400, Fredericton, NB, Canada E3B 5A3

ABSTRACT

Bubble flow is characterised by numerous phase interfaces and turbulence, leading to fast magnetic resonance signal decay and artefacts in spin-warp imaging. In this paper, the SPRITE MRI pulse sequence, with its potential for very short encoding times, is demonstrated as an ideal technique for studying such dynamic systems. It has been used to acquire liquid velocity and relative intensity maps of two-phase gas–liquid dispersed bubble flow in a horizontal pipe at a liquid Reynolds number of 14,500. The fluids were air and water and a turbulence grid was used to generate a dispersed bubble flow pattern. The SPRITE technique shows promise for future research in gas–liquid flow.

© 2009 Published by Elsevier Inc.

1. Introduction

1.1. Gas–liquid two-phase pipe flow

Two-phase gas–liquid flow occurs in many situations of theoretical and practical interest. One of the most common geometries is pipe flow, particularly in hydrocarbon processing, boilers and cooling systems. As with all multiphase flows it is a complex phenomenon and current measuring and modelling capabilities are limited; consequently there are presently no generally applicable CFD codes available [1]. The online measurement of bulk flow rates alone in such systems is difficult and measuring local phase distributions and velocities is even more challenging. There is a need for techniques that can measure local parameters for two reasons: first, to improve our fundamental understanding of gas–liquid flow; and second, to validate CFD codes. Major motivations for studying such systems are to learn how different phase and velocity distributions influence pressure drop and corrosion.

The fundamentals of gas–liquid flow are presented here but a more comprehensive account can be found in standard texts, for example Perry et al. [2] and Coulson et al. [3]. The distribution of phases in gas–liquid flow depends on the relative flow rates, fluid properties and geometries, and can be classified into a number of distinct patterns or flow regimes. Gravity causes the less dense gas phase to rise (buoyancy); therefore the direction of gravity relative to the flow axis means that vertical and horizontal pipe flows exhibit different behaviour and in the latter the gas phase tends to

occupy the upper part of the pipe. As the gas-to-liquid ratio increases the gas changes from forming the dispersed phase to the continuous phase. Flow regime definitions are subjective and the transitions between them are gradual, but in general seven flow regimes for fully-developed horizontal pipe flow have been identified [4], as illustrated in Fig. 1. They are as follows, in order of decreasing ratio of liquid to gas flow rate:

Bubbly flow. The gas is dispersed in the liquid as bubbles which move at a velocity similar to the liquid. This flow regime occurs at high ratios of liquid to gas flow rates, but note that gravitational forces will tend to cause the bubbles to concentrate near the top of the pipe at lower liquid velocities and the distribution of bubbles becomes more homogeneous at higher liquid velocities.
Plug flow. Alternate plugs of liquid and gas move along the upper part of the pipe.
Stratified flow. The liquid and gas flow along the bottom and top of the pipe respectively, with a smooth interface.
Wavy flow. This is similar to stratified flow but waves moving in the flow direction are formed at the gas–liquid interface because of higher relative velocities between the phases.
Slug flow. Liquid waves touch the top of the surface of the pipe, forming frothy slugs which move at a velocity much greater than the liquid average velocity.
Annular flow. Liquid flows as a thin film along the pipe walls and gas flows in the core with some entrained droplets of liquid.
Spray, dispersed or mist flow. This is similar to annular flow except nearly all the liquid phase is entrained as small droplets.

* Corresponding author. Fax: +1 506 453 4581.
  E-mail address: bnewling@UNB.ca (B. Newling).

Nomenclature

A	pipe cross-sectional area (m)	z	Cartesian z-coordinate (m)
$\mathbf{B}_0$	static magnetic field (T)		
g	magnetic field gradient strength (flow-encoding) (T m^{-1})	*Greek symbols*	
I	MR signal intensity (a.u.)	γ	gyromagnetic ratio (T^{-1} s^{-1})
$\mathbf{k}$	reciprocal space dimension (field gradients) (m^{-1})	Δ	observation time between flow gradients (s)
Q	volumetric flow rate (m^3 s^{-1})	δ	duration of flow gradient (s)
$\mathbf{q}$	reciprocal space dimension (flow gradients) (m^{-1})	ε	phase fraction
T_1	spin-lattice (longitudinal) relaxation time (s)	$\langle \bar{\varepsilon} \rangle$	time- and volume-averaged phase fraction
T_2	spin-spin (transverse) relaxation time (s)		
T_2^*	modified spin-spin (transverse) relaxation time (s)	*Subscripts*	
t_p	phase-encoding time (s)	i	subscript indicating fluid phase
U	superficial velocity (m s^{-1})	G	gas phase
u	*in situ* velocity (m s^{-1})	L	liquid phase
x	Cartesian x-coordinate (m)	single	single-phase flow
y	Cartesian y-coordinate (m)	two	two-phase flow

These regimes can be conveniently plotted as a function of gas and liquid flow rate in the form of a flow pattern map, the first of which was created by Baker [5] and is still widely used. Some authors have developed mechanistic models, using different procedures for estimating pressure drop and void fraction for each flow pattern. These are more accurate for predicting flow pattern transitions than flow maps, especially for conditions deviating from small diameter pipes of air–water flow at atmospheric pressure. Barnea [6] presented a unified model for the whole range of pipe inclinations and published analytical and empirical equations for determining flow regime transitions.

The bubbly flow pattern also occurs in vertical flow but at much lower velocities than those observed for horizontal flow. Barnea [6] makes a distinction between "dispersed bubble flow" and "bubbly flow". The latter occurs at low liquid velocities only in relatively large diameter tubes close to the vertical orientation, while the former occurs at high liquid velocities at all angles of pipe inclination. This is the definition for "dispersed bubble flow" used in this paper. Horizontal two-phase flow has received less attention in the literature than vertical, not least because the migration of bubbles towards the top of the pipe presents challenges for experimental observation. However, dispersed bubble flow is found in cooling
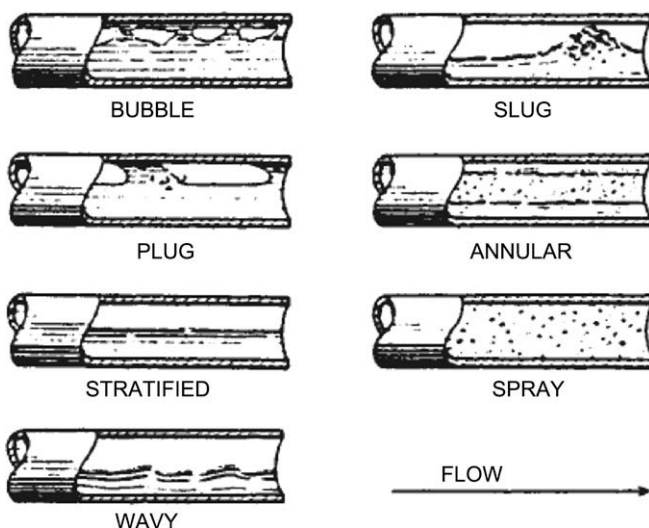

Fig. 1. Gas–liquid flow patterns in horizontal pipes (reproduced with permission, copyright American Institute of Chemical Engineers, from Alves [4]).

pipes, and the stratified flow regime is extremely important in long-distance pipelines [1].

The gas phase always flows at a greater velocity than the liquid phase in pipes (slip), therefore the *in situ* volume fraction of gas is less than the input volume fraction of gas. However, the gas volume fraction will progressively increase along the pipe flow direction as the gas expands due to the reduction in pressure caused by friction and other losses. For each phase denoted by subscript i, flowing with volumetric flow rate Q_i, volume phase fraction ε_i and *in situ* velocity u_i through a pipe of cross-sectional area A, the following equation defines the superficial velocity, U_i:

$$Q_i = \int_A u_i \varepsilon_i \, dA = U_i A \quad i = \mathrm{L, G} \tag{1}$$

Lockhart and Martinelli [7] published a correlation for estimating liquid volume fraction (holdup) in fully-developed horizontal two-phase flow. They also developed a method for estimating the frictional pressure drop in two-phase flow and correlated experimental pressure drop data with an accuracy of ±50%.

1.2. Tomography and velocimetry

Knowledge of the spatially-resolved phase distribution is crucial for characterising and understanding multiphase flow systems. A number of methodologies exist for measuring void fraction and velocities in two-phase gas–liquid flow. The simplest way to measure holdup is to isolate a section of pipe with valves and determine the volume of liquid trapped, but this method is clearly imprecise and invasive. For a thorough explanation of the more advanced tomography techniques that have been applied to gas–liquid pipe flow, the reader is referred to the reviews by Chaouki et al. [8] and Reinecke et al. [9]. Here, some of these techniques are classified and briefly reviewed, with a list of applications in Table 1:

Optical techniques, *e.g.* visual observation in real-time or with a high speed camera, Particle Imaging Velocimetry (PIV), Laser Doppler Anenometry (LDA), Phase Doppler Anenometry (PDA). These methods have a high spatial and temporal resolution but require the system to be transparent and refractive index-matched, which is problematic for two-phase flows, particularly flows with dispersed bubbles or a high void fraction. PIV requires that tracer particles be added.
Invasive techniques, *e.g.* hot wire anemometry (HWA), hot film anemometry (HFA), conductance probes, electrodiffusion. These

Table 1
Tomographic visualisations of two-phase gas–liquid pipe flows. Flow regimes are abbreviated as follows: B = bubble, DB = dispersed bubble and S = slug.

Reference	Technique	Fluids	Regime	Properties measured	Diameter (mm)	Orientation
[27]	Conductance probes	Air–water	DB	Bubble size	18 50	Horizontal
[15]	MRI	Air–water	B	Void fraction	25	Vertical
[13]	MRI	Air–water	S	Liquid fraction; liquid velocity probability distribution	49	Vertical
[14]	MRI	Air–water	S	Void fraction; liquid velocity	29	Vertical
[28]	PIV	Air–water + tracer	B	Instantaneous liquid velocity field, turbulence intensity, Reynolds stress	11	Vertical
[29]	HFA	Air–water	DB	Void fraction; bubble passing frequency; liquid turbulence fluctuations	50	Horizontal
[30]	Electro-diffusion, conductivity, visual observation	Air–water + ions	DB	Liquid velocity; bubble concentration	20	Vertical
[31]	XPTV	Glycerol + tracer	B	Liquid velocity	104	Vertical
[19]	Resistivity probe, high speed cinematography	Air–water	DB	Void fraction; interfacial area concentration; bubble passing frequency; bubble interface velocity; bubble size distribution	50	Horizontal
[12]	MRI	Air–water	B	Void fraction; liquid velocity propagator; liquid flow rate fluctuation	50	Vertical
[32]	CT, conductivity mesh	Air–water	B, S	Void fraction	42	Vertical
[33]	LDA, HFA	Air–water	B	Liquid velocity	102	Vertical
[34]	Conductance probes	Air–water	B	Void fraction; interfacial area and velocity; bubble diameter	102	Vertical
[35]	Doppler ultrasound	Air–water	B	Liquid and bubble rise velocities	30	Vertical
[36]	HFA	Air–water	B	Liquid velocity and turbulent fluctuations	35	Horizontal

can give local velocities and void fractions but the probe or mesh interferes invasively with the flow.

Electrical tomography, *e.g.* electrical capacitance tomography (ECT), electrical resistance tomography (ERT). These are non-invasive, suitable for opaque systems and have a high temporal resolution, but have a very low spatial resolution and rely on complex reconstruction algorithms and considerable prior knowledge.

Radiation tomography, *e.g.* neutron radiography, X-ray Computer Tomography (CT), X-ray Particle Tracking Velocimetry (XPTV), Neutron radiography can measure void fraction with an exposure time of a few seconds but cannot be used for velocity measurement; X-ray CT can measure almost instantaneous void fraction but requires relatively complex reconstruction algorithms; XPTV uses X-ray CT to measure velocities by tracking particles.

Other techniques, *e.g.* Doppler ultrasound, magnetic resonance (MR). Doppler ultrasound can obtain velocity data but is limited to flows with a very low gas holdup and requires tracer particles to be added. MR is discussed in detail below.

1.3. Magnetic resonance applied to bubble flow

MR is experiencing increased use for characterising multiphase flows, because it has a number of key advantages over other techniques for two-phase flow tomography. It is completely non-invasive, but unlike optical methods it can be used to study optically opaque systems. In addition, it can be rendered sensitive to a range of parameters, including spin density, relaxation times, chemical shift, rates of diffusion and coherent flow velocities. Magnetic Resonance Imaging (MRI), thanks to the use of magnetic field gradients, returns spatially-resolved information with a potential resolution of <100 μm. Most MRI data can be processed by Fourier transformation without the need for complex reconstruction algorithms. The disadvantages of MRI include a relatively low spatial or temporal resolution compared to some other techniques (although this depends on the system analysed and pulse sequence employed), restricted sample geometry imposed by the need for a strong homogeneous magnetic field, the inability to image magnetic materials and difficulties associated with very heterogeneous materials (although the SPRITE method described below is relatively robust in this last case).

A number of magnetic resonance studies of bubble flow are in the literature, all of air–water flows in a vertical pipe. Lynch and Segel [10] used continuous wave (CW) NMR spectroscopy to measure volume-averaged void fraction in a vertical bubble column and demonstrated the linear relationship between NMR signal intensity and void fraction. Abouelwafa and Kendall [11] used CW NMR spectroscopy to measure the volume fraction and individual flow rates of two-component water–oil and water–air mixtures. Leblond et al. [12] used Pulsed Field Gradient Spin Echo (PFGSE) NMR to measure volume-averaged void fraction, liquid velocity propagators and turbulence fluctuations in steady-state bubble flow as well as the time evolution of flow under a transient condition. Barberon and Leblond [13] used time-averaged spatially-resolved PFGSE MRI to demonstrate the existence of a recirculatory flow under a Taylor slug bubble, while Gladden et al. [14] employed the GERVAIS ultrafast velocity imaging sequence to obtain instantaneous velocity maps of liquid flow in the same system. As a proof-of-concept, Daidzic et al. [15] used a permanent magnet MRI system and a spin-warp pulse sequence to make spatially-resolved time-averaged measurements of gas void fraction in a stagnant column of water. Their data showed the quantitative linear agreement (within ±15%) between MRI-measured void fraction and macroscopically-measured gas flow rate up to a void fraction of around 0.4. The low field strength reduced distortion due to magnetic susceptibility but some phase artefacts were observed because of the time-varying void distribution. All of the above were in the vertical orientation; to the best of the authors' knowledge there have been no MRI studies of horizontal gas–liquid flow and no spatially-resolved velocity mapping of dispersed bubble flow.

1.4. SPRITE MRI

The SPRITE MRI technique [16] uses single-point imaging (SPI) and pure phase-encoding instead of conventional spin-warp frequency-encoding. This confers certain advantages: (i) SPRITE can successfully image fast flows (*i.e.* with a velocity >1 m s^{-1}); (ii) it can image samples with low values of T_2^* such as fluorinated gases, solids and heterogeneous systems with numerous phase interfaces (such as those present in two-phase flows); (iii) it is not affected by artefacts in the time-domain, *e.g.* those caused by chemical shift or magnetic susceptibility differences. Furthermore, it has been shown that, when combined with centric **k**-space sampling, SPRITE can give a robust and quantitative measure of spin density without

the influence of other factors such as diffusion, shear or relaxation [17]. In general the sequence is designed to promote signal-to-noise ratio (SNR) and spin density quantification at the expense of spatial resolution. SPRITE is usually used to study dynamics on the order of seconds to hours, not as a snapshot technique. However, it is suitable for steady-state systems and those that can be described by time-averaged properties (e.g. turbulence). Therefore SPRITE represents a promising technique for visualising two-phase flows. The aim of this paper is to demonstrate the ability to acquire maps of liquid velocity and estimate gas void fraction for bubbly flow in a horizontal pipe using SPRITE MRI.

2. Experimental method

2.1. Apparatus

All MRI measurements were performed using a MARAN-DRX 7T spectrometer (Resonance Instruments, Witney, UK) operating at a ^{1}H frequency of 300 MHz with a 160 mm bore actively screened magnet system (Magnex Scientific, Oxford, UK) and a 400 W NMR-plus model 8T400 radio-frequency (RF) power amplifier (Communication Power, Brentwood, NY, USA). Magnetic field gradients of up to 40 G cm^{-1} were provided by a self-shielded Magnex gradient set, SGRAD 156/100/S. A home-built birdcage RF resonator of internal diameter 6.2 cm was used for both radiofrequency transmission and reception, tuned to the ^{1}H frequency with a 90° pulse length of 60 μs.

The liquid used was deionised water (density = 997 kg m^{-3}, dynamic viscosity = 0.001 Pa s at 295 K) doped with 8.0 mM GdCl$_3$ in order to lower the T_1 and T_2 relaxation times to 8.4 and 6.5 ms, measured using inversion recovery and CPMG pulse sequences respectively [18]. The T_1 relaxation time was chosen to satisfy the condition that the fastest flowing water spins had enough time (at least $5 \times T_1$) in the $\mathbf{B}_0$ field to become polarised before they reached the RF coil. A short T_2 time also reduces the degree of homospoiling required to destroy residual transverse magnetisation between each single point acquisition. The water was transported from a reservoir vessel by a flexible vane pump. The gas was air from a compressor regulated at an inlet pressure of 1 barg. Rotameters were used to measure the flow rates of both the liquid (Brooks Instrument Canada Ltd, Hatfield, PA, USA; model number 8-1305) and the gas (Brooks; Sho-rate tube size 2-65) before mixing.

The bubble flow was formed by combining the gas and liquid flows in a mixing chamber (Fig. 2) with the gas dispersed into bubbles through a glass sinter. The pump was not capable of generating liquid velocities high enough for spontaneous dispersed bubble flow, so a dispersion of bubbles was created by passing the two-phase mixture through a grid of polyurethane foam. The fluids then entered a straight section of glass tubing of internal diameter 13.9 mm that passed through the imaging region (a length of 120 mm starting 50 mm downstream of the grid). On leaving the spectrometer the fluids entered the reservoir vessel whereupon the air was released to the atmosphere and the water was recycled back into the flow loop. See Fig. 2 for a schematic of the mixing device, including the assignment of Cartesian coordinate directions, and Fig. 3 for a schematic of the flow loop. Because of the short distance from the grid to the imaging section, the flow was not fully-developed and is only analogous to dispersed bubble flow. It should be noted that Kocamustafaogullari and Huang [19] state that a fully-developed bubbly two-phase flow pattern cannot actually be established in horizontal flow because of the buoyancy effect. They also comment that the bubble size is determined by the degree of turbulence in the system which is the principle exploited by the turbulence-generating grid.
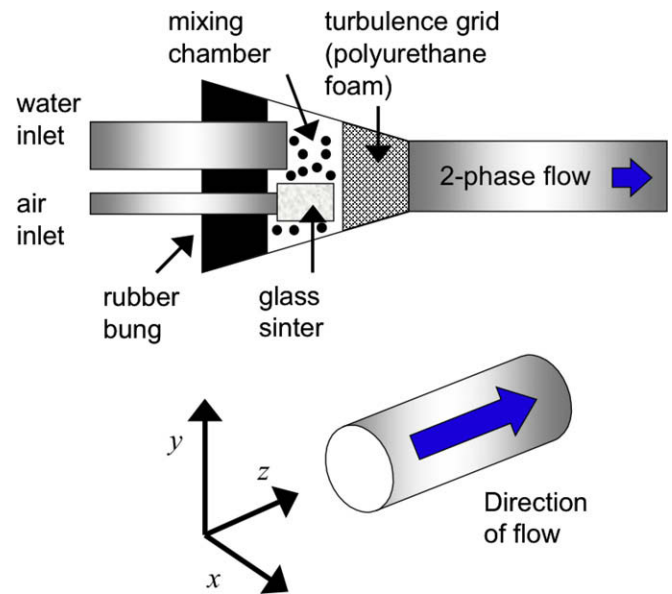

Fig. 2. A schematic of the two-phase mixing device showing the assigned Cartesian coordinate directions.
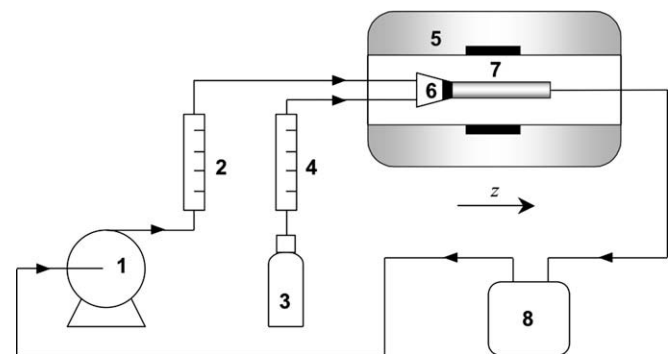

Fig. 3. Schematic of the apparatus. 1, Pump; 2, liquid rotameter; 3, compressed air supply (regulated at 1 barg); 4, gas rotameter; 5, 7 T superconducting magnet; 6, bubble mixing device; 7, test section; 8, separation vessel/liquid reservoir.

2.2. Experiments

Velocity data were acquired using a motion-sensitised version of the SPRITE technique which employed bipolar pulsed field gradients, superimposed upon the ramped imaging gradients, for flow-encoding. This was initially demonstrated by Newling et al. [20] but the sequence as employed in the current work features two modifications. The first is that $\mathbf{k}$-space is traversed using the Sectoral sampling scheme which reduces blurring compared to the Spiral or Conical trajectories [21]. The second modification is that a time delay was inserted between the two lobes of the bipolar flow gradient pair (shown in Fig. 4), which allows for gradient stabilisation and gives more control over the gradient timings. The flow-encoding gradients can be superimposed in any direction to measure that component of the velocity. Two position-encoding gradients were applied to generate 2D images that are a projection in the third orthogonal direction (there is no slice selection). Note that spatial-encoding in this third direction was not incorporated into the pulse sequence because of the increased experimental time; this is due to both an increase in the number of data points to acquire and an increase in the number of scans required to give the same signal-to-noise ratio.
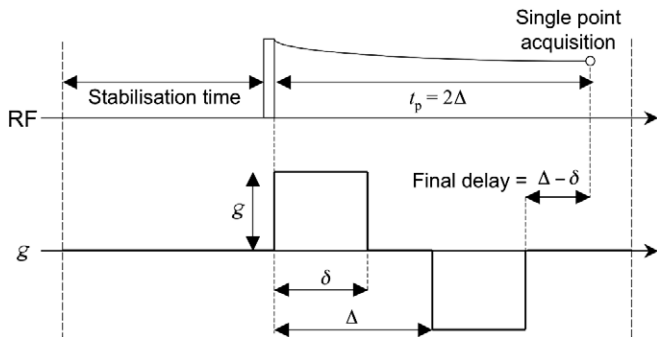
Fig. 4. Part of the motion-sensitised SPRITE pulse sequence, indicating the sequence timings. The section shown is for the acquisition of a single data point and corresponds to the interval between position-encoding gradient ramps (omitted).

Experiments were conducted on single-phase liquid flow and two-phase bubbly flow at the same liquid flow rate. Liquid signal intensity and velocity were mapped in both the z–x and z–y orientations for each two-phase flow regime and for single-phase liquid flow. Data were not acquired in the x–y orientation because this would have entailed a projection in the z-direction through the inhomogeneous regions of applied gradient. (The $\mathbf{B}_0$ and $\mathbf{B}_1$ are also potentially inhomogeneous over this projection, but the gradient effect is most significant, SPRITE being very robust in the presence of inhomogeneous $\mathbf{B}_0$.) In all cases a 2D image matrix of size 64×64 voxels was acquired with a field-of-view of 40 mm in the x- or y-directions and 120 mm in the z-direction. The maximum strengths of the position-encoding gradients were 1.85 G cm^{-1} in the x- and y-directions and 6.17 G cm^{-1} in the z-direction. Eight sampling sectors were used. The RF pulse angle was 10°, corresponding to a pulse length of 6.67 μs. The phase-encoding time, t_p, between the pulse and the corresponding single point acquisition was 1 ms for the signal intensity images and 1.3 ms for the velocity images. There was also an interval of 5 ms between each single point acquisition and the next RF pulse: this gives time for stabilisation of the position-encoding gradients and spoiling of the residual signal. Each image was acquired with a single scan in a time of approximately 30 s.

The signal intensity maps used the SPRITE sequence described above with a flow gradient strength $g = 0$. They are maps of time-averaged liquid holdup because no signal is received from regions of gas (void space). The time and volume-averaged void fraction can be obtained by calculating the ratio of the MRI signal intensity in two-phase gas–liquid flow, I_{two}, with that in single-phase liquid flow only, I_{single}:

$$\langle \bar{\varepsilon}_G \rangle = 1 - \langle \bar{\varepsilon}_L \rangle = 1 - \frac{I_{two}}{I_{single}} \qquad (2)$$

Eq. (2) is based on the assumption that there is no loss of signal due to dephasing in magnetic field gradients and also no appreciable change in T_2^*; this will be discussed later.

Each velocity experiment comprised eight 2D images acquired with different values of g ranging from $-g_{max}$ to $(3/4\ g_{max})$, where $g_{max} = 20.1$ G cm^{-1}. The flow gradient parameters (defined in Fig. 4) were $\delta = 350$ μs and $\Delta = 650$ μs. Each image was composed of a 64×64 array of **k**-space data which was Fourier-transformed in the two spatial directions. The eight images were zero-filled to 64 points and Fourier-transformed in the third direction to yield a data set with two spatial dimensions and one displacement dimension, *i.e.* a set of spatially-resolved displacement probability distributions, also known as propagators [18]. Displacements were converted to time-averaged velocities by division by Δ. The value of the flow velocity assigned to each voxel in a 2D velocity map

was the location of the peak in the propagator, constraining the velocity maps to have 64 velocity bins of width 32.0 mm s^{-1}.

3. Results and discussion

3.1. Visual observation

The flow regime at a number of different gas and liquid flow rates was photographed in order to study the behaviour of the system visually (Fig. 5). The bubble pattern becomes more dispersed with increasing liquid flow rate. SPRITE MRI was then used to acquire 2D liquid fraction and velocity maps and maps at one liquid flow rate (0.16 kg s^{-1}) and two different gas flow rates[1] (4.2×10^{-4} kg s^{-1} and 8.6×10^{-4} kg s^{-1}). The liquid superficial velocity was 1.0 m s^{-1}, corresponding to a Reynolds number (based on the pipe diameter) of 14,500. The pressure in the imaging section was slightly above atmospheric due to the frictional pressure drop down the pipe. Based on this, the gas superficial velocities were 2.1 and 3.9 m s^{-1}.

3.2. Relaxation measurements

Global T_2^* values of the liquid were taken from biexponential fits to the FIDs. These were (64% 0.32 ms and 36% 3.9 ms) when the liquid was stationary, (54% 0.33 ms and 46% 3.2 ms) in single-phase flow and (66% 0.37 ms and 34% 1.7 ms) for two-phase flow at the higher gas flow rate. These short signal lifetimes in dispersed bubble flow, caused by the numerous phase interfaces and the corresponding increase in local field inhomogeneity, highlight the necessity of using SPRITE for this application. These bulk values are somewhat affected by $\mathbf{B}_1$ inhomogeneities at the end of the RF probe and (in the case of the flowing fluids) by inflow/outflow effects upon signal.

3.3. Void fraction

Relative signal intensity images (I_{two}/I_{single}, Eq. (2)) for the low and high gas flow rates are given in Figs. 6 and 7 respectively, along with data for single-phase liquid flow for comparison. Image intensity is clearly locally governed by both void fraction and T_2^* as our $t_p = 1$ ms is not sufficiently short to completely remove the effects of local T_2^* variation. Our choice of t_p was conservative and there is considerable scope for t_p reduction (see Section 3.5).

In the bubble flow, the z–x (horizontal) distribution is symmetrical as expected. The z–y (vertical) distribution shows a vertical gradient due to buoyancy effects which cause the phases to separate as they move along the pipe. The increased gas flow rate in Fig. 7 is evident in the more pronounced void fraction distribution, as well as the higher background signal level (due to greater void and velocity fluctuation, which causes some smearing of the image, see below and [22]). A slight periodic intensity fluctuation is discernible in the images in the z-direction; this is an artefact, which we believe due to residual transverse magnetisation [23], and is the subject of further investigation. The average void fractions (neglecting T_2^*) measured from I_{two}/I_{single} were 0.17 and 0.27 for the low and high gas flow rates respectively. These cannot be validated by standard two-phase flow correlations because the flow was not fully-developed. Transverse magnetisation decay during the phase-encoding time reduces the measured liquid signal which means the amount of liquid is underestimated and thus the void fraction is overestimated.

---

[1] Among the optical photographs, Fig. 5f is closest to the conditions measured with MRI (at the lower gas flow rate of 4.2×10^{-4} kg s^{-1}).
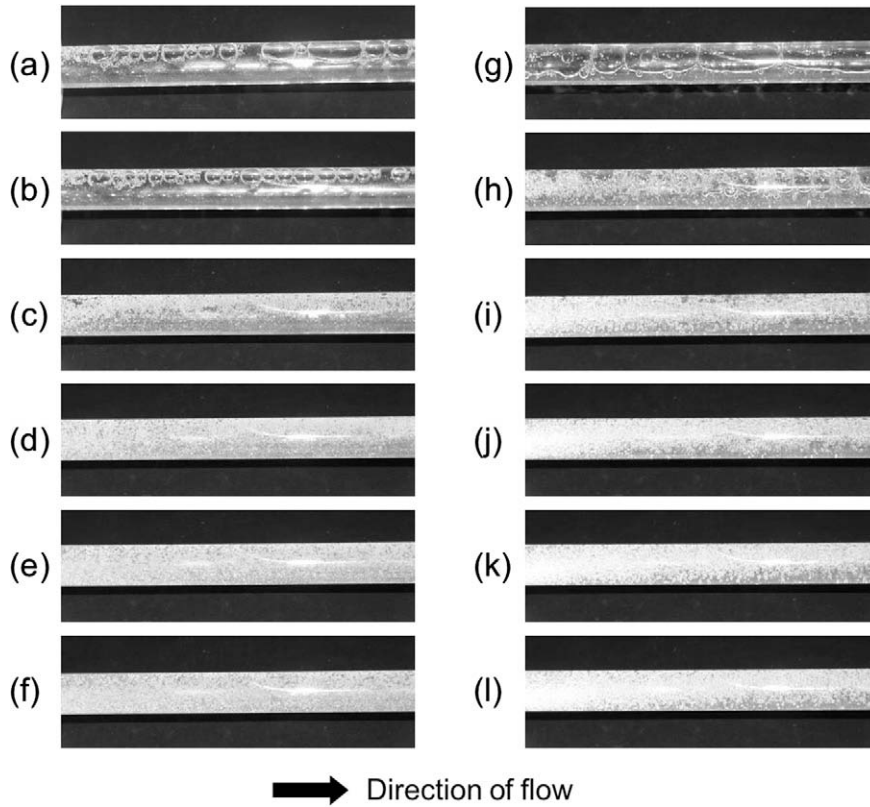
Fig. 5. Optical photographs of different flow regimes. The gas mass flow rate [10^{-4} kg s^{-1}] is (a)–(f) 4, (g)–(l) 40. The liquid mass flow rate [kg s^{-1}] is (a) 0.044, (b) 0.076, (c) 0.101, (d) 0.126, (e) 0.136, (f) 0.142, (g) 0.038, (h) 0.069, (i) 0.095, (j) 0.107, (k) 0.120 and (l) 0.132. The bubble pattern becomes more dispersed with increasing liquid flow rate.
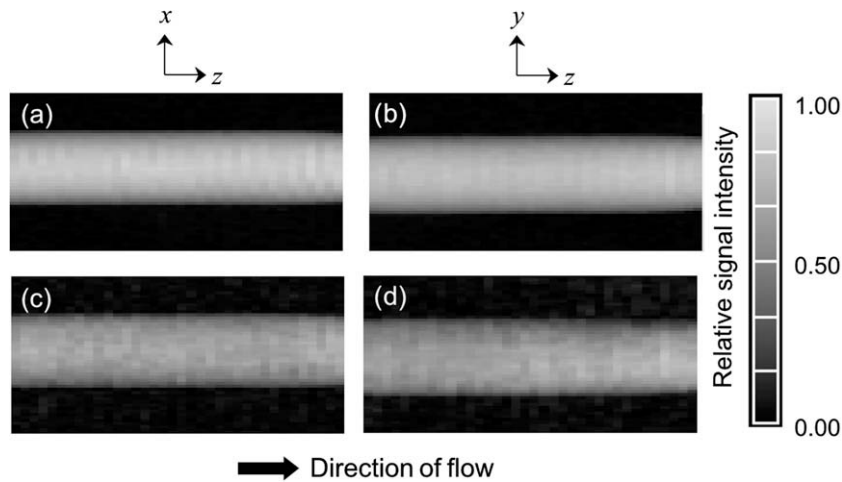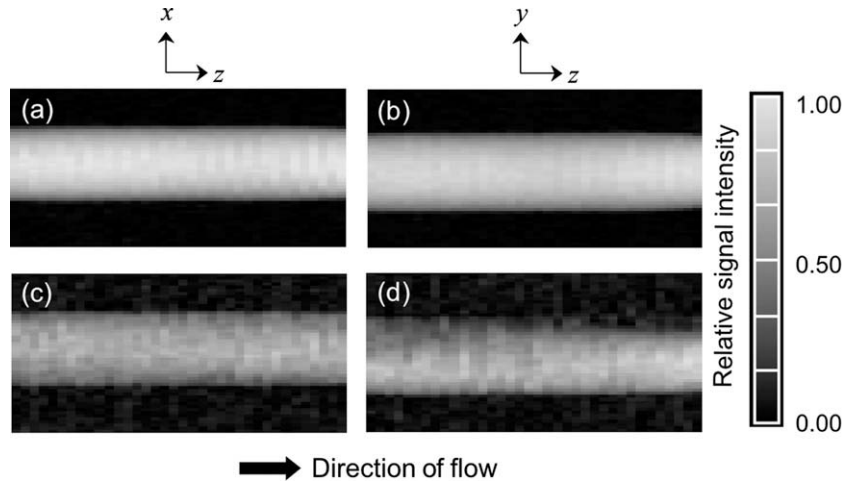

Fig. 6. (a and b) Images of single-phase liquid flow and (c and d) relative signal intensity images (I_{two}/I_{single}, see Eq. (2)) of bubble flow. (a and c) z–x (horizontal) plane; (b and d) z–y (vertical) plane. The mass flow rate of liquid is 0.16 kg s^{-1} in both cases, corresponding to a superficial velocity of 1.0 m s^{-1}; the mass flow rate of gas is 4.2×10^{-4} kg s^{-1}.
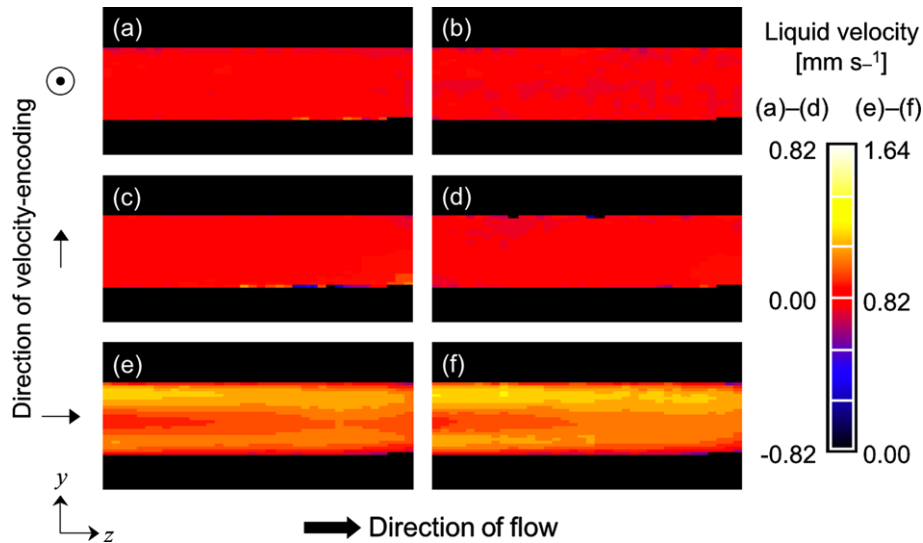
3.4. Velocity maps

Velocity maps for the low gas flow rate are given in Figs. 8 and 9 (z–y and z–x orientations respectively) and for the high gas flow rate in Figs. 10 and 11 (z–y and z–x orientations respectively). For single-phase flow in both orientations, the x-velocity and y-velocity maps are approximately zero, while the z-velocity map is close to symmetrical about the pipe axis as expected. Deviations in the latter, particularly the faster jets at the top and bottom of the

pipe in the z–y orientation, are caused by asymmetry in the mixing chamber geometry and the turbulence grid. For two-phase flow, the x-velocity map is approximately zero in both orientations as expected. The y-velocity and z-velocity maps show evidence of the gas phase rising to the top of the pipe due to buoyancy effects. This effect is least obvious in the z–y orientation because of projection across the tube along the x axis. The z–y orientation z-velocity map shows how the presence of bubbles increases the liquid z-velocity in the upper part of the pipe due to the higher void frac-

Fig. 7. (a and b) Images of single-phase liquid flow and (c and d) relative signal intensity images (I_{two}/I_{single}, see Eq. (2)) of bubble flow. (a and c) z–x (horizontal) plane; (b and d) z–y (vertical) plane. The mass flow rate of liquid is 0.16 kg s^{-1} in both cases, corresponding to a superficial velocity of 1.0 m s^{-1}; the mass flow rate of gas is 8.6×10^{-4} kg s^{-1}.

Fig. 8. Velocity maps of (a, c and e) single-phase liquid flow and (b, d and f) bubble flow. The mass flow rates of liquid and gas are 0.16 kg s^{-1} and 4.2×10^{-4} kg s^{-1} respectively. The data are 2D projections in the z–y (vertical) plane and are maps of (a and b) x-velocity, (c and d) y-velocity, and (e and f) z-velocity.

tion. The z–x orientation z-velocity map is more asymmetrical than the equivalent in single-phase flow, presumably because the presence of the gas phase accentuates any horizontal asymmetry in the apparatus. These observations can be made for both gas flow rates, but the faster gas flow causes a greater gas buoyancy effect and therefore a wider range of z-velocities. The average liquid superficial velocity values calculated from the MRI data were 0.97 m s^{-1} for all the velocity maps, both for single- and two-phase flow. This compares favourably with the superficial velocity of 1.0 ($\pm$0.1) m s^{-1} measured using the rotameter.

3.5. Potential improvements to the measurement

Due to the fast gradient switches used, the actual gradient shapes applied may differ from the perfect theoretical shapes expected. This is most likely to affect the flow gradients because the gradient strengths were of the order of 10 times higher than the position gradients. The gradient stabilisation delay of 5 ms before each RF pulse was intended to reduce this error. However, the delay between the two lobes of the flow-encoding bipolar pair was necessarily much less ($\Delta - \delta = 300$ μs) in order to shorten t_p. An alternative solution (not employed here) would be to use carefully shaped gradient pulses. We deemed use of the propagator mode the best analysis for control of uncertainty in our velocity maps. However, these low resolution measurements may very well benefit from optimisation with a cumulant analysis [24].

The amount of transverse signal decay that occurs before the acquisition of a data point depends on the length of the phase-encoding time. Shorter encoding times give less signal decay and a more accurate measure of the true spin density of the voxel. The t_p value of 1.3 ms for the velocity maps cannot easily be reduced because of the time required for a flow-encoding gradient pair, but there is scope to reduce the t_p of the spin density images to a value less than the 1 ms used. In this case, some spoiling of the suspected residual transverse magnetisation or increased doping of the sample (where possible) might be necessary. Definitive measurement of void fraction by MRI will require multiple t_p acquisitions and independent validation using stopped-flow volume measurements, for example.
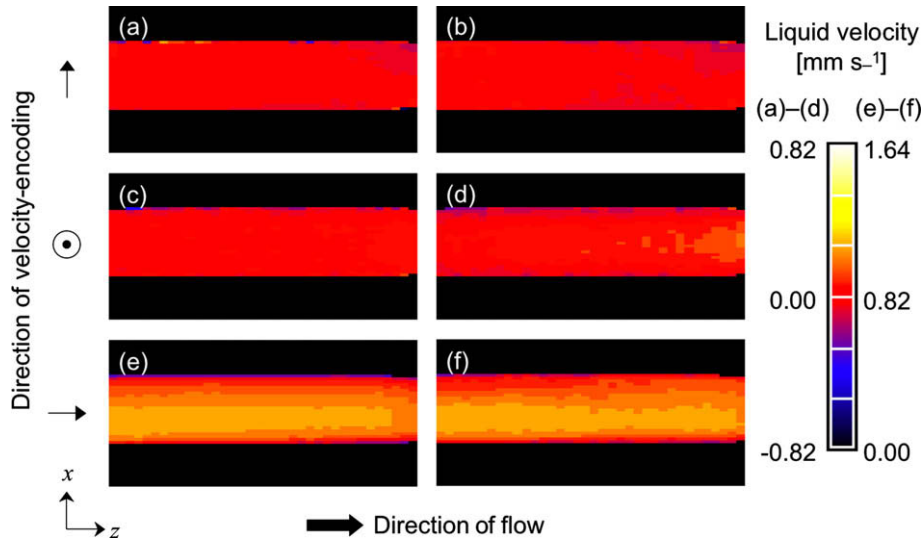
Fig. 9. Velocity maps of (a, c and e) single-phase liquid flow and (b, d and f) bubble flow. The mass flow rates of liquid and gas are 0.16 kg s^{-1} and 4.2 × 10^{-4} kg s^{-1} respectively. The data are 2D projections in the *z*–*x* (horizontal) plane and are maps of (a and b) *x*-velocity, (c and d) *y*-velocity, (e and f) *z*-velocity.
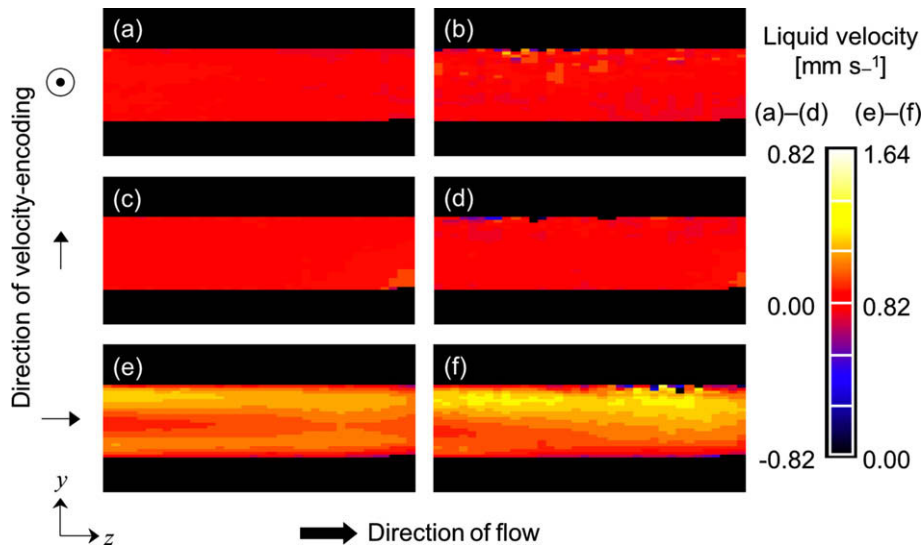
Fig. 10. Velocity maps of (a, c and e) single-phase liquid flow and (b, d and f) bubble flow. The mass flow rates of liquid and gas are 0.16 kg s^{-1} and 8.6 × 10^{-4} kg s^{-1} respectively. The data are 2D projections in the *z*–*y* (vertical) plane and are maps of (a and b) *x*-velocity, (c and d) *y*-velocity, (e and f) *z*-velocity.

3.6. Sample fluctuations

SPRITE is a time-averaged technique suitable for steady-state systems. The bubble flow system shows long-term steady-state behaviour but there are short-term fluctuations in the void distribution. This may lead to artefacts and blurring in the images which are generated from a Fourier transformation of data points acquired with different void distributions. The nature of the artefacts depends on the relative magnitude of the fluctuations and also how their frequency compares with the pulse sequence timing. There are two fundamental timing parameters in the SPRITE sequence: the phase-encoding time and the recycle time between RF pulses. Sample fluctuations will have occurred during both these time scales, but visual observation suggests that their magnitude is low and not likely to distort the data significantly. In this regard SPI has two advantages over spin echo techniques: first, the time between excitation and acquisition is very short; and second, the pure phase-encoding means any artefacts are distributed across the image, not concentrated in a line like the "phase artefact" characteristic of spin-warp imaging of fluctuating systems (such as that demonstrated by [22]). It would be interesting to conduct further research on this effect by a combination of experimental work and computational simulation.

4. Conclusions

This work has demonstrated the ability of SPRITE MRI to acquire approximate void fraction and quantitative liquid velocity maps of gas–liquid dispersed bubble flow in a horizontal pipe. The short encoding time and pure phase-encoding nature of the technique are particularly well suited to this system. The 2D data are averaged over the transverse direction of the pipe which limits their resolution but it is a trivial extension to acquire 3D data by adding a position gradient in the third orthogonal direction [21]. The data are time-averaged over minutes of acquisition and any parameters which might be derived from the data, such as bubble size distribu-
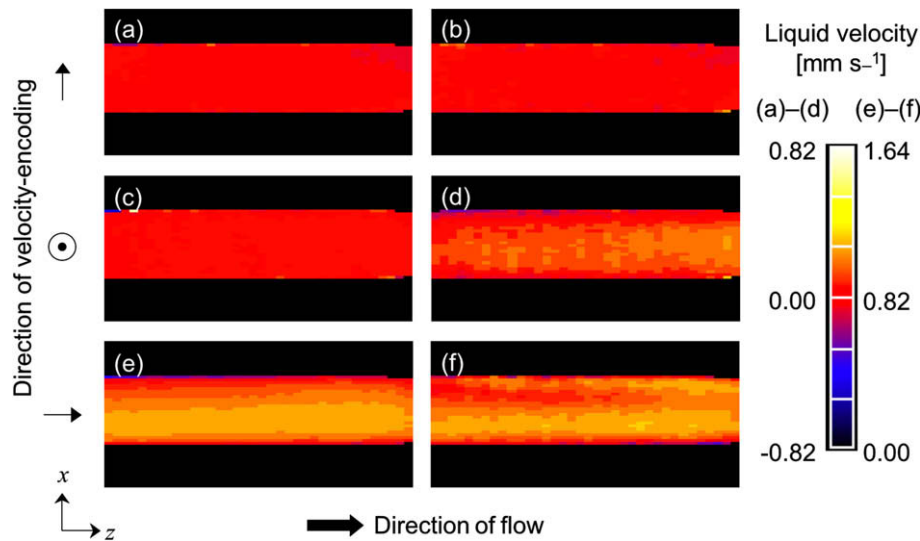
Fig. 11. Velocity maps of (a, c and e) single-phase liquid flow and (b, d and f) bubble flow. The mass flow rates of liquid and gas are 0.16 kg s^{-1} and 8.6 × 10^{-4} kg s^{-1} respectively. The data are 2D projections in the z–x (horizontal) plane and are maps of (a and b) x-velocity, (c and d) y-velocity, (e and f) z-velocity.

tions from rise velocities, are similarly averaged. There are a number of developments that could be made to improve the results and applicability of the technique. It would be possible to image the gas signal intensity and velocity directly by using an MR-active gas species, *e.g.* SF$_6$ [25,26]; using two RF coils to detect different MR-active nuclei in each phase it would be possible to acquire data for the gas and liquid phases simultaneously. The flow apparatus could be improved by using a more powerful pump to obtain higher liquid superficial velocities and hence generate dispersed bubble flow without the use of a turbulence grid; in this case at least 50 pipe diameters of straight pipe should be included before the imaging section to allow fully-developed flow. It will also be valuable to investigate flow around obstructions and bends which may help explain flow-accelerated corrosion effects. Finally, the data acquired by SPRITE MRI could be used to validate multiphase CFD modelling, a technology still in its infancy.

Acknowledgments

References

[1] S. Ghorai, K.D.P. Nigam, CFD modeling of flow profiles and interfacial phenomena in two-phase flow in pipes, Chem. Eng. Process. 45 (2006) 55–65.
[2] R.H. Perry, D.W. Green, J.O. Maloney, Perry's Chemical Engineers' Handbook, seventh ed., McGraw-Hill, New York, London, 1997.
[3] J.M. Coulson, J.F. Richardson, R.K. Sinnott, Coulson & Richardson's Chemical Engineering, Butterworth-Heinemann, Oxford, 1999.
[4] G.E. Alves, Cocurrent liquid–gas flow in a pipeline contractor, Chem. Eng. Prog. 50 (1954) 449–456.
[5] O. Baker, Simultaneous flow of oil and gas, Oil Gas J. 53 (1954) 85–195.
[6] D. Barnea, A unified model for predicting flow-pattern transitions for the whole range of pipe inclinations, Int. J. Multiphase Flow 13 (1987) 1–12.
[7] R.W. Lockhart, R.C. Martinelli, Proposed correlation of data for isothermal two-phase. Two-component flow in pipes, Chem. Eng. Prog. 17 (1949) 553–572.
[8] J. Chaouki, F. Larachi, M.P. Duduković, Noninvasive tomographic and velocimetric monitoring of multiphase flows, Ind. Eng. Chem. Res. 36 (1997) 4476–4503.
[9] N. Reinecke, G. Petritsch, D. Schmitz, D. Mewes, Tomographic measurement techniques – visualization of multiphase flows, Chem. Eng. Technol. 21 (1998) 7–18.
[10] G.F. Lynch, S.L. Segel, Direct measurement of void fraction of a 2-phase fluid by nuclear magnetic-resonance, Int. J. Heat Mass Transfer 20 (1977) 7–14.
[11] M.S.A. Abouelwafa, E.J.M. Kendall, Optimization of continuous wave nuclear magnetic-resonance to determine in situ volume fractions and individual flow-rates in 2 component mixtures, Rev. Sci. Instrum. 50 (1979) 1545–1549.
[12] J. Leblond, S. Javelot, D. Lebrun, L. Lebon, Two-phase flow characterization by nuclear magnetic resonance, Nucl. Eng. Design 184 (1998) 229–237.
[13] F. Barberon, J. Leblond, Intermittent two-phase flow study by NMR, C. R. De L Acad. Des Sci. Serie Ii Fascicule C Chim. 4 (2001) 853–856.
[14] L.F. Gladden, B.S. Akpa, L.D. Anadón, J.J. Heras, D.J. Holland, M.D. Mantle, S. Matthews, C. Mueller, M.C. Sains, A.J. Sederman, Dynamic MR imaging of single- and two-phase flows, Chem. Eng. Res. Design 84 (2006) 272–281.
[15] N.E. Daidzic, E. Schmidt, M.M. Hasan, S. Altobelli, Gas–liquid phase distribution and void fraction measurements using MRI, Nucl. Eng. Design 235 (2005) 1163–1178.
[16] B.J. Balcom, R.P. MacGregor, S.D. Beyea, D.P. Green, R.L. Armstrong, T.W. Bremner, Single-point ramped imaging with T-1 enhancement (SPRITE), J. Magn. Res. Ser. A 123 (1996) 131–134.
[17] I.V. Mastikhin, B.J. Balcom, P.J. Prado, C.B. Kennedy, SPRITE MRI with prepared magnetization and centric k-space sampling, J. Magn. Res. 136 (1999) 159–168.
[18] P.T. Callaghan, Principles of Nuclear Magnetic Resonance Microscopy, Clarendon Press, Oxford, 1991.
[19] G. Kocamustafaogullari, W.D. Huang, Internal structure and interfacial velocity development for bubbly 2-phase flow, Nucl. Eng. Design 151 (1994) 79–101.
[20] B. Newling, C.C. Poirier, Y. Zhi, J.A. Rioux, D. Coristine, D. Roach, B.J. Balcom, Velocity imaging of highly turbulent gas flow, Phys. Rev. Lett. 93 (2004).
[21] A.A. Khrapitchev, B. Newling, B.J. Balcom, Sectoral sampling in centric-scan SPRITE magnetic resonance imaging, J. Magn. Res. 178 (2006) 288–296.
[22] M.C. Sains, M.S. El-Bachir, A.J. Sederman, L.F. Gladden, Rapid imaging of fluid flow patterns in a narrow packed bed using MRI, Magn. Res. Imaging 23 (2005) 391–393.
[23] C.B. Kennedy, B.J. Balcom, I.V. Mastikhin, Three dimensional magnetic resonance imaging of rigid polymeric materials using single point ramped imaging with T$_1$ enhancement (SPRITE), Can. J. Chem. 76 (1998) 1763–1765.
[24] U.M. Scheven, J.P. Crawshaw, V.J. Anderson, R. Harris, M.L. Johns, L.F. Gladden, A cumulant analysis for non-Gaussian displacement distributions in Newtonian and non-Newtonian flows through porous media, Magn. Res. Imaging 25 (2007) 513–516.
[25] M.H. Sankey, D.J. Holland, A.J. Sederman, L.F. Gladden, Magnetic resonance velocity imaging of liquid and gas two-phase flow, J. Magn. Res., 2008. doi:10.1016/j.jmr.2008.10.0201.
[26] B. Newling, Gas flow measurements by NMR, Prog. Nucl. Magn. Res. Spectrosc. 52 (2008) 31–48.
[27] P. Andreussi, A. Paglianti, F.S. Silva, Dispersed bubble flow in horizontal pipes, Chem. Eng. Sci. 54 (1999) 1101–1107.

[28] Y.A. Hassan, W. Schmidl, J. Ortiz-Villafuerte, Investigation of three-dimensional two-phase flow structure in a bubbly pipe flow, Meas. Sci. Technol. 9 (1998) 309–326.
[29] A. Iskandrani, G. Kojasoy, Local void fraction and velocity field description in horizontal bubbly flow, Nucl. Eng. Design 204 (2001) 117–128.
[30] O.N. Kashinsky, P.D. Lobanov, M.A. Pakhomov, V.V. Randin, V.I. Terekhov, Experimental and numerical study of downward bubbly flow in a pipe, Int. J. Heat Mass Transfer 49 (2006) 3717–3727.
[31] U. Kertzscher, A. Seeger, K. Affeld, L. Goubergrits, E. Wellnhofer, X-ray based particle tracking velocimetry – a measurement technique for multi-phase flows and flows without optical access, Flow Meas. Instrum. 15 (2004) 199–206.

[32] H.M. Prasser, M. Misawa, I. Tiseanu, Comparison between wire-mesh sensor and ultra-fast X-ray tomograph for an air–water flow in a vertical pipe, Flow Meas. Instrum. 16 (2005) 73–83.
[33] X. Sun, S. Kim, T.R. Smith, M. Ishii, Local liquid velocity measurements in air–water bubbly flow, Exp. Fluids 33 (2002) 653–662.
[34] X.D. Sun, T.R. Smith, S. Kim, M. Ishii, J. Uhle, Interfacial area of bubbly flow in a relatively large diameter pipe, Exp. Therm. Fluid Sci. 27 (2002) 97–109.
[35] T.F. Wang, J.F. Wang, F. Ren, Y. Jin, Application of Doppler ultrasound velocimetry in multiphase flow, Chem. Eng. J. 92 (2003) 111–122.
[36] J. Yang, M.Y. Zhang, C.J. Zhang, Y.L. Su, X.R. Zhu, Quasi 3-D measurements of turbulence structure in horizontal air–water bubbly flow, Nucl. Eng. Design 227 (2004) 301–312.